Review article

Taehee Kang*, Young-Mi Bahk* and Dai-Sik Kim*

Terahertz quantum plasmonics at nanoscales and angstrom scales

https://doi.org/10.1515/nanoph-2019-0436
Received October 20, 2019; revised December 8, 2019; accepted December 16, 2019

Abstract: Through the manipulation of metallic structures, light–matter interaction can enter into the realm of quantum mechanics. For example, intense terahertz pulses illuminating a metallic nanotip can promote terahertz field–driven electron tunneling to generate enormous electron emission currents in a subpicosecond time scale. By decreasing the dimension of the metallic structures down to the nanoscale and angstrom scale, one can obtain a strong field enhancement of the incoming terahertz field to achieve atomic field strength of the order of V/nm, driving electrons in the metal into tunneling regime by overcoming the potential barrier. Therefore, designing and optimizing the metal structure for high field enhancement are an essential step for studying the quantum phenomena with terahertz light. In this review, we present several types of metallic structures that can enhance the coupling of incoming terahertz pulses with the metals, leading to a strong modification of the potential barriers by the terahertz electric fields. Extreme nonlinear responses are expected, providing opportunities for the terahertz light for the strong light–matter interaction. Starting from a brief review about the terahertz field enhancement on the metallic structures, a few examples including metallic tips, dipole antenna, and metal nanogaps are introduced for boosting the quantum phenomena. The emerging techniques to control the electron tunneling driven by the terahertz pulse have a direct impact on the ultrafast science and on the realization of next-generation quantum devices.

***Corresponding authors: Taehee Kang and Dai-Sik Kim,** Department of Physics, Ulsan National Institute of Science and Technology (UNIST), Ulsan 44919, Korea, e-mail: taehee.kang@mbi-berlin.de (T. Kang); daisikkim@unist.ac.kr (D.-S. Kim); and
Young-Mi Bahk, Department of Physics, Incheon National University, Incheon 22012, Korea, e-mail: ymb@inu.ac.kr.
https://orcid.org/0000-0001-7039-3135

Keywords: terahertz spectroscopy; quantum plasmonics; nanostructures; electron tunneling.

1 Introduction

Over the past decades, advances in the generation of intense terahertz waves have enabled new researches on light–matter interaction. In particular, tabletop systems generating high-power terahertz pulses [1–6] provide broad opportunities to study ultrafast dynamics of matters in the nonlinear regime, through resonant and nonresonant coupling [7–18]. The low photon energy of terahertz waves allows resonant coupling with direct excitation of low-energy modes such as vibrations of crystal lattices, rotation of molecules, precessions of spins, and internal excitations of bound electron–hole pairs. Therefore, when the strong terahertz field is incident on the matter, it causes numerous low-energy excitations with large amplitudes beyond harmonic response. In addition to resonant manipulation, high electric field in a picosecond time scale can provide long-enough acceleration of free electrons and transient barrier distortion with strong voltage within a half cycle of driving field. This permits that the electron overcomes energy barriers of bound states. This light-field–driven tunneling can lead to interesting phenomena such as terahertz field emission [15, 19, 20], high harmonic generation [18, 21, 22], and nonlinear transmission [13, 14, 16, 23] by making a dramatic change of material properties arising from the whole distortion of electronic potential without damaging the material due to the picosecond time scale of the terahertz pulses.

On the other hand, recent development of nanofabrication technology brings a large impact on various photonic researches including terahertz plasmonics [24–33]. Artificially designed metal structures in subwavelength scale are used to manipulate the response of the terahertz field, realizing a wide range of applications in sensors [30, 31, 34–37], switches [38–41], and filters [42–45]. Especially, a perfect conductor-like behavior of the noble metals in terahertz frequency

range makes possible for strong light–matter interaction with nanoscale metal gaps or point geometries [26, 46–50]. Electric field enhancement factor can reach a few thousands by coupling light with the metal structure, paving a way to study extreme nonlinear phenomena and providing ideal platform for the terahertz quantum plasmonics. Designing the metal nanostructures has therefore a significant impact on the terahertz responses in the quantum regime.

Terahertz quantum plasmonics is a research field that involves the studies of the quantum properties of light and its interaction with matter at nanoscale and angstrom scale in terahertz frequency regime. In this review, we focus on a nonresonant terahertz nonlinear phenomenon of electron tunneling driven by intense terahertz radiation that plasmonic metal nanostructures provide. We introduce a few basic building blocks of the metal nanostructures: a tip, coupled tips (dipole antenna), and metal gap for efficient generation of tunneling electrons driven by the terahertz waves. Meeting with the strong terahertz pulses, the metal nanostructures can enhance the electron tunneling, thereby leading to various extreme phenomena and useful applications.

2 Terahertz field enhancement in various metal structures

Metal structures such as nanotip, nanoantennas, and nanoslit and slot antennas have been of great research interest over the past two decades because of their potentials and functionalities for a broad range of applications such as chemistry, biology, and medical applications, as well as from basic research aspects [24, 51–64]. Strong field enhancement and confinement obtained at the subwavelength volume are the main resultant properties from interaction between electromagnetic waves and metal nanostructure, which are essential for nonlinear optics in nanoscale.

Figure 1 shows various metal nanostructures, nanotip (Figure 1A), nanoantenna (Figure 1B and C), nanoslit (Figure 1D), and nanoslot antenna (Figure 1E). Basically, the large field enhancement originates from the tight focusing of the terahertz electric field near the tip apex or at the nanogap induced by charge accumulation and capacitive coupling (Figure 1F) [26, 69]. These two physical phenomena, charge accumulation and capacitive coupling, not

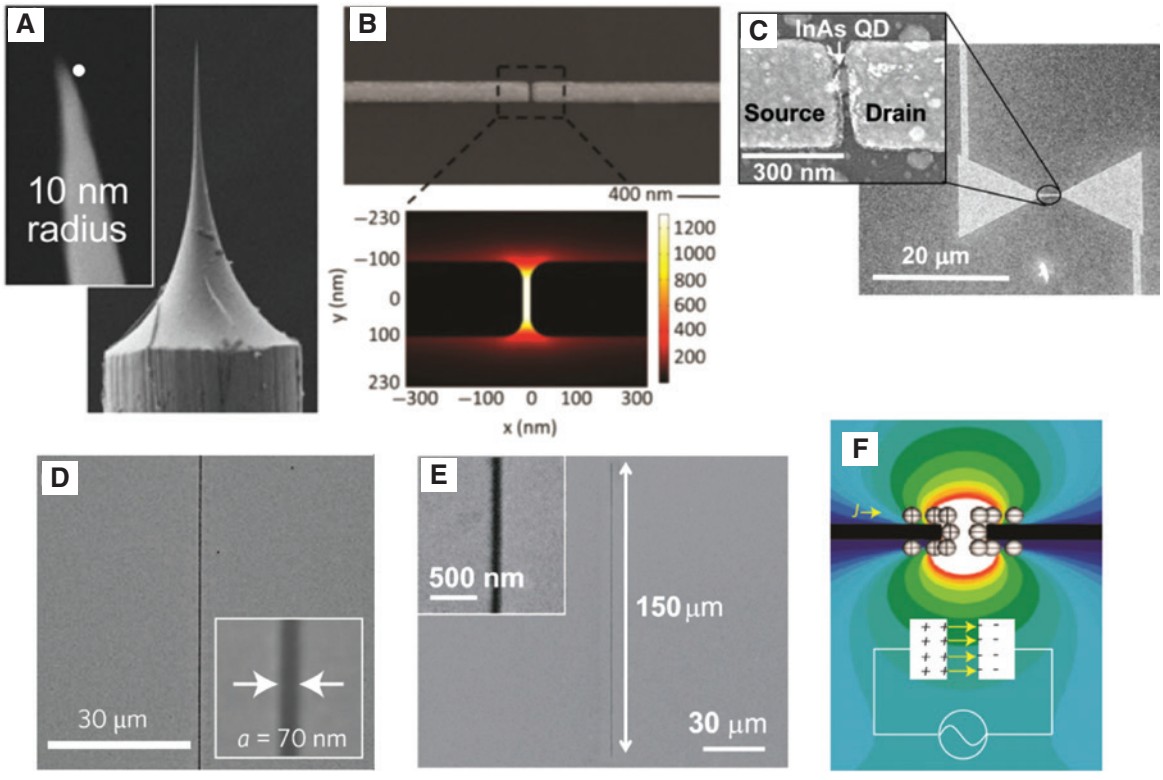

Figure 1: Metal nanostructures for strong field enhancement and confinement of terahertz waves.
(A–E) SEM images of metal nanotip (A), dipole antenna (B), bowtie-shaped nanoantenna (C), nanoslit (D), and nanoslot antenna (E), respectively. (F) Enhanced electric field distribution induced by charge accumulation and capacitive coupling in metal nanogap. The figures are reproduced from References [26, 65–68].

necessarily of an orthogonal nature to each other, allow us to explain the efficiency of field enhancement in a broad spectral range from visible light to microwaves [70–72]. Beyond the broadband spectral response of nanotip and nanoslit, dipole antennas and slot antennas are employed for the resonant excitation, furthering the capacities for manipulation and control of spatially and temporally localized electrons. In the next section, we will review recent progress in ultrafast control of electrons using terahertz plasmonics, which is one of the most studied terahertz nonlinear optics that requires intense electromagnetic field.

3 Terahertz field–induced quantum electron tunneling

Tunneling is one of the most fundamental quantum mechanical phenomena; wave function of matters can penetrate and eventually transmit through a classically forbidden potential barrier. Strong electrical bias on the metal surface applied by the terahertz pulse excitation modifies the barrier and can emit electrons from the metal. This tunneling current directly affects the experiments exploiting strong terahertz pulsed sources with metal nanostructures, and we therefore need to consider the tunneling phenomena quantitatively when analyzing the data.

When a terahertz electric field is incident on two metallic electrodes separated by a thin insulating film, electrons can flow through the potential barrier by tunneling effect (Figure 2). Tunneling current density J across a one-dimensional barrier by applying potential difference V at 0 K is given by [73, 74]

$$J(V)=\frac{4\pi me}{h^3}\left[\int_0^{E_f} D(E)(\eta-E)\mathrm{d}E-\int_0^{E_f-eV} D(E)(E_f-eV-E)\mathrm{d}E\right] \quad (1)$$

where m is the electron mass; e, the electron charge; h, the Plank constant; E_f, the Fermi level of the metal; E, the tunneling electron energy; $D(E)=\exp(-4\pi\Delta w(2m(\eta+\phi_m-E))^{1/2}/h)$, the tunneling probability factor calculated by WKB approximation; $\phi_m=\int_{w_1}^{w_2}(\phi(x)+\phi_i(x))dx/\Delta w$, the mean value of the barrier height; $\phi(x)=\phi-eVx/w$, the barrier potential profile affected by the THz electric field; $\phi_i(x)=-1.15e^2w^2\ln(2)/16\pi\varepsilon wx(w-x)$, the approximated form of barrier modification by image force; w, the thickness of the insulating layer; ε, the dielectric constant of the insulating layer; and $\Delta w=w_2-w_1$ is the effective barrier width, where w_1 and w_2 are acquired from the zeros of $\phi(x)+\phi_i(x)=0$. Because of the exponential dependence for the applied electric field V/w, the tunneling current exhibits a highly nonlinear character. For example, even a 1-nm increase for a 1-nm gap with a constant voltage (or the field strength reduced by half while fixing the gap size) changes the tunneling current by several orders of magnitudes smaller.

The first term of (1) indicates tunneling current from electrode 1 (left) to electrode 2 (right) where the energy level of electrode 2 is lowered by amount of eV, and the second term indicates the current flowing in a reverse direction. When the applied field is strong enough to suppress the Fermi level of electrode 2 below the bottom of conduction band of electrode 1, i.e. $eV>E_f$, electrons cannot tunnel from electrode 2 to electrode 1 because of the absence of available states. In this case, the second term of (1) can be neglected and J can be written by

$$J(V)\propto\frac{V^2}{\phi w^2}\exp\left(-C\frac{\phi^{3/2}}{V}w\right) \quad (2)$$

with a constant C, which is the Fowler–Nordheim tunneling formula for field emission from a single metallic electrode [75]. In this case of field emission, the barrier potential denotes the work function of the metal.

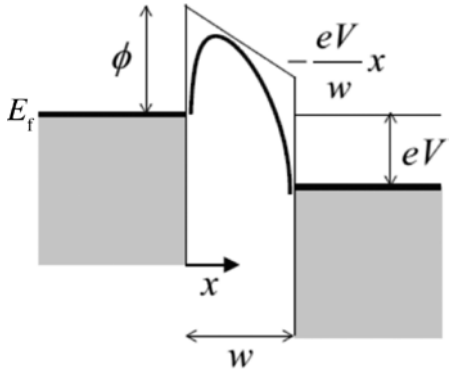

Figure 2: Potential barrier with height ϕ across an insulating layer width of w sandwiched between two metallic films. Electrons in the conduction band under Fermi level E_f for each metallic electrode can tunnel through the barrier. Applied bias V by the incoming terahertz field distorts the barrier profile asymmetrically, thereby the current flowing from left to right. The figure is reproduced from Reference [13].

3.1 Metal nanotip

3.1.1 Terahertz scanning tunneling microscope

Terahertz scanning tunneling microscope (STM) (THz-STM) is capable of imaging surfaces with atomic spatial resolution and the subpicosecond time resolution (<0.5

ps), much faster than conventional STM system [15, 17, 19, 20, 76, 77]. The basic principle of THz-STM is quantum tunneling through the gap between the tip and sample resulting from a transient voltage induced by terahertz pulses. The total time-dependent voltage across the tunnel junction is the sum of the DC bias voltage and the terahertz pulse-induced transient voltage (left of Figure 3B). Because of the nonlinear characteristic of current–voltage relation in the tunnel junction, a time-dependent tunneling current with a rectified component is produced (right of Figure 3B). The terahertz-induced tunneling current pulses result in the time-averaged shift in STM current–voltage curves.

The spatial resolution limited by diffraction of terahertz waves (~1 mm) can be overcome by a scanning probe tip, which is an atomically sharp metallic tip with the resolution on the order of 10 nm. The free-space traveling terahertz pulses are focused on the STM tip acting as a broadband antenna [78, 79] that couples the electric field of the terahertz pulses to the tip–sample junction via a Sommerfeld mode [80]. The strongly enhanced terahertz electric field at the tip apex enables to produce the transient bias voltage with maintaining nanometer spatial resolution. A recent work reports imaging and tunneling spectroscopy of conductive surfaces with atomic resolution (~0.3 nm), which shows the image of ultrafast nonequilibrium tunneling dynamics for individual atoms on a silicon surface [17].

The antenna-like coupling of terahertz waves to the metal nanotip in STM system also results in polarization-dependent current–voltage characteristic. Figure 3C shows the STM current–voltage curves for a bare, flat, highly ordered pyrolytic graphite (HOPG) sample, revealing that the terahertz pulse generates an increased tunnel

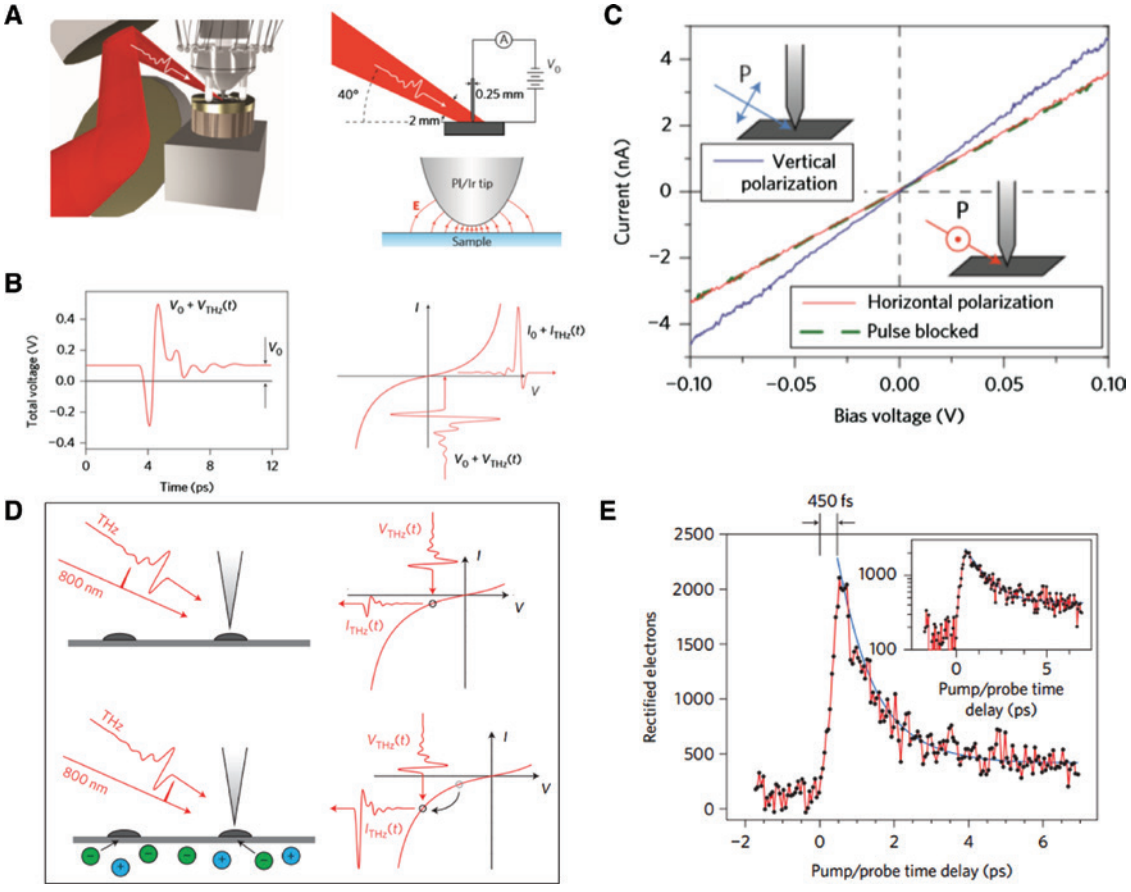

Figure 3: Ultrafast THz-STM system.
(A) Schematics of THz-STM system. A terahertz pulse propagating through free-space couples to an STM tip, and the electric field of terahertz pulse is strongly confined and enhanced at the metal tip apex. (B) The total voltage across the tip–sample junction as a function of time (left) and the nonlinear curve of tunnel current and voltage (right). The transient voltage induced by terahertz pulse results in the transient tunnel current with a rectified component. (C) The average tunnel current as a function of bias voltage measured in HOPG sample with terahertz polarization parallel (blue line) and transverse (red line) to the STM tip. Terahertz pulses produce an increased tunnel current only for the polarization parallel to the STM tip. The green dashed line is current–voltage curve with terahertz beam blocked. (D) Schematics of optical-pump THz-STM–probe system. The terahertz-induced tunnel current with a different rectified component is measured before and after photoexcitation. (E) Time-resolved optical-pump THz-STM–probe signal for single InAs nanodots where the rise time is ~500 fs, and the decay time is ~1 ps. The figures are reproduced from Reference [19].

current only when the electric field of the terahertz pulse is polarized parallel to the metal tip [78–80].

The THz-STM system is used to study ultrafast carrier dynamics of single nanoparticles in subpicosecond time resolution by combining pump–probe technique. The terahertz-induced tunnel current with a different rectified component before and after optical excitation is measured by optical-pump THz-STM–probe system as seen in Figure 3D. Figure 3E is the change of tunnel current caused by photoexcitation in InAs nanodot as a function of pump–probe time delay. After photoexcitation, the electron trapping into InAs nanodots increases local bias voltage. resulting in the increase of rectified component in tunnel current. In the time-resolved THz-STM signal, the rise time of ~500 fs and the decay time of ~1 ps were measured with a nanoscale spatial resolution [19]. Also, by introducing pump–probe technique where one terahertz pulse (pump) modifies transiently the rectified currents induced by the second one (probe), the ultrafast dynamics of an individual molecule such as a coherent vibration of the molecules was visualized in real space with an atomic scale [15].

In the THz-STM system, the single-cycle terahertz electric field transiently produces asymmetric bias voltage based on DC bias voltage, leading to the rectified component of tunnel current. In turn, the rectified tunnel current direction in the tip–sample junction is determined by the DC bias voltage because of the symmetric terahertz pulse shape in time domain. By using carrier–envelope phase (CEP)–controlled terahertz electric fields, the tunnel electrons in the tip–sample junction can be manipulated coherently. To experimentally control the CEP of single-cycle terahertz electric field, a pair of cylindrical lenses or spherical lenses for $\pi/2$ or π phase change, respectively (Figure 4A). The CEP-controlled terahertz electric field leads to the coherent distortion of potential barrier directly (Figure 4B). For the symmetric terahertz pulse, the direction of ultrafast electron tunneling is determined by the DC bias voltage, where the electrons tunnel from the metal tip (sample) to the sample (metal tip) under a positive (negative) DC bias voltage. In case of the asymmetric terahertz pulses, however, ultrafast tunnel current induced by strong terahertz field has unidirectional behavior while sweeping the DC bias voltage from negative to positive

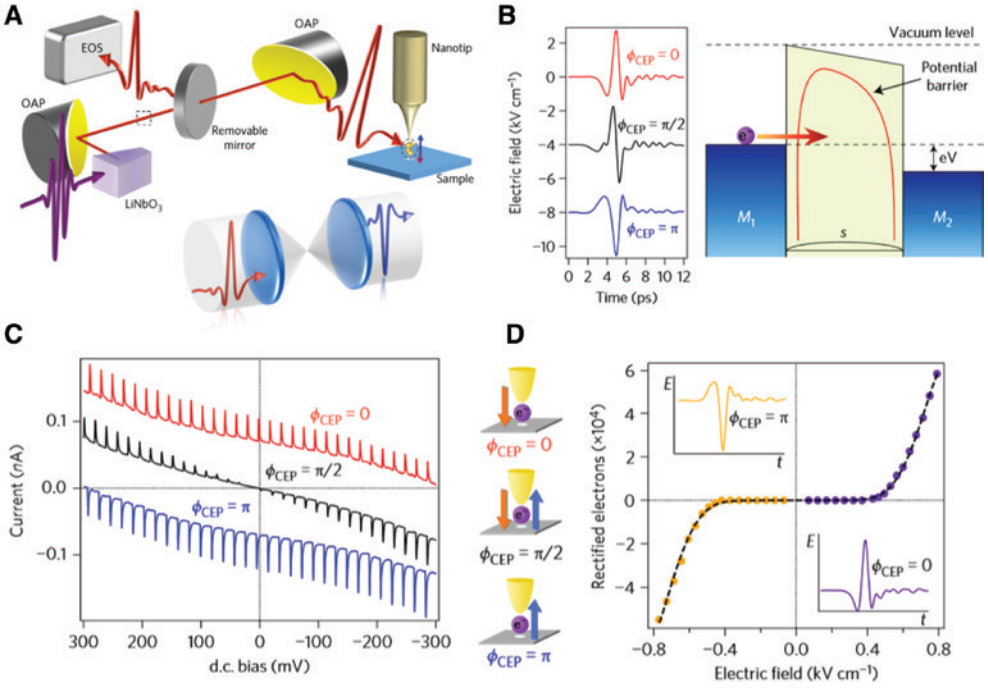

Figure 4: THz-STM system based on CEP–controlled terahertz fields.
(A) Schematic of THz-STM setup. The incident terahertz pulse is focused onto the metal nanotip and coupled via antenna-like plasmonic effect. The CEP of single-cycle terahertz pulse is controlled by a pair of cylindrical or spherical lenses. (B) Terahertz electric fields in time domain with different CEP (0, $\pi/2$, and π), which show half- (red and blue lines) and single-cycle (black line) terahertz electric fields (left). The CEP-controlled terahertz electric field modifies potential barrier between metal tip and sample (right). (C) The tunnel current as a function of DC bias voltage in the tip–sample junction for different CEP terahertz electric fields. (D) Schematic of electron motion between the metal nanotip to sample for different CEP (left) and terahertz field–induced rectified electrons as a function of peak field of terahertz pulse (right). The CEP-controlled terahertz field leads to the unidirectional coherent motion of electrons. The figures are reproduced from Reference [20].

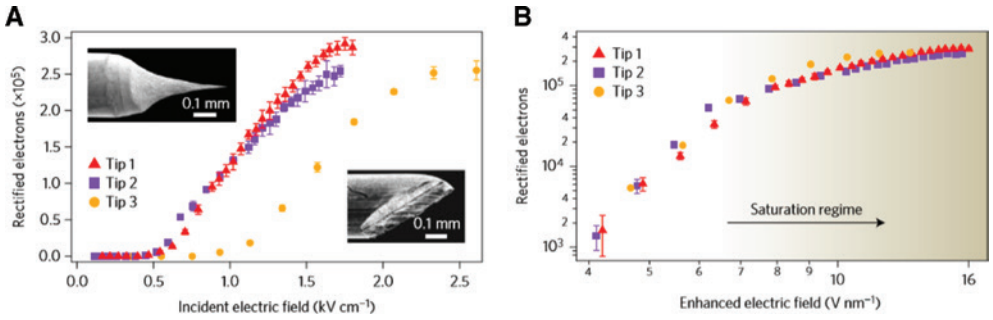

Figure 5: Rectified electrons from the nanotip.
(A) Number of rectified electrons as a function of incident terahertz electric field, measured with three different metal tips. Electrochemical etching produces sharp tips (Tips 1 and 2), whereas mechanical cutting makes a blunt tip (Tip 3). Insets are SEM images of sharp (top) and blunt (bottom) tips. (B) Number of rectified electrons as a function of enhanced terahertz electric field for three different tips, in which the same behavior indicates that the tip geometry affects only the enhancement factor. The saturation regime (space-charge-limited regime) is achieved by strong field enhancement in metal nanotip. The figures are reproduced from Reference [20].

value. The direction of ultrafast tunneling current strongly depends on the CEP of terahertz pulses (Figure 4C, D).

This coherent manipulation of electron motion is enabled by terahertz-induced bias voltage, which is strong enough to distort barrier height in the tip–sample junction. The strong transient voltage is induced by the large field enhancement realized by the broadband antenna effect in the metal nanotip. Therefore, for the shaper metal tip accompanying stronger field enhancement and confinement, the larger tunnel current is measured in a given incident terahertz electric field (Figure 5A). It is worth to note that the rectified electrons show the same curves as a function of electric field scaled by enhancement factor, indicating that the tip geometry plays an important role to reach strong field regime at a given incident field (Figure 5B). Furthermore, the strong field enhancement by metal nanotip assists to reach a new regime, an extremely high-voltage regime where an additional space-charge potential plays an important role in the strong saturation of the tunneling electrons.

3.1.2 Terahertz field emission

Terahertz field emission is one of terahertz field–driven processes enabled by the high field enhancement in metal nanotip. Figure 6A shows the experimental setup of terahertz-induced field emission from a sharp tungsten tip in high-vacuum condition (10^{-8} mbar range), in which an incident single-cycle terahertz pulse is focused by an off-axis parabolic mirror and the emitted electrons are detected by a time-of-flight (TOF) electron spectrometer and a microchannel plate detector. The enhanced transient terahertz pulses created by antenna-like coupling of metal tip induce nonlinear electron emission from the nanotip, through ac-tunneling into vacuum and acceleration process by the locally enhanced terahertz near field. The emitted electron kinetic energy distributions are characterized by transient strong terahertz field. Figure 6C displays TOF spectra for two different terahertz pulse strengths. The spectral shape stems from nonlinear emission at maximum field strength and subsequent acceleration in the terahertz-induced momentary potential. Another recent work reported that large local field enhancement of terahertz pulses in metal nanotips is responsible for producing electrons with energies exceeding 5 keV, via terahertz field–driven electron emission process [81].

Tip-enhanced single-cycle terahertz pulse can be used for control of photoelectron dynamics in dual-frequency excitation of metal nanotip. For example, assisted by optical field enhancement, near-infrared pulses (800-nm wavelength) induce nonlinear photoelectron emission from the nanotip, which is gated and streaked by the enhanced terahertz electric field (Figure 6D, E). This near-field streaking technique can be applicable for nanoscopic version of terahertz streaking device [47].

3.2 Metal nanoantenna

3.2.1 Photon-assisted tunneling in single-molecule transistors

Electron transport through single molecules has been intensively studied because of its potential for device applications such as single-electron transistor. Beyond static properties of the single-electron transistor, its dynamical transport properties have been investigated by terahertz waves because typical energy scales in single-molecule transport lie mostly in the terahertz frequency regime such as tunneling times, vibron energies, orbital

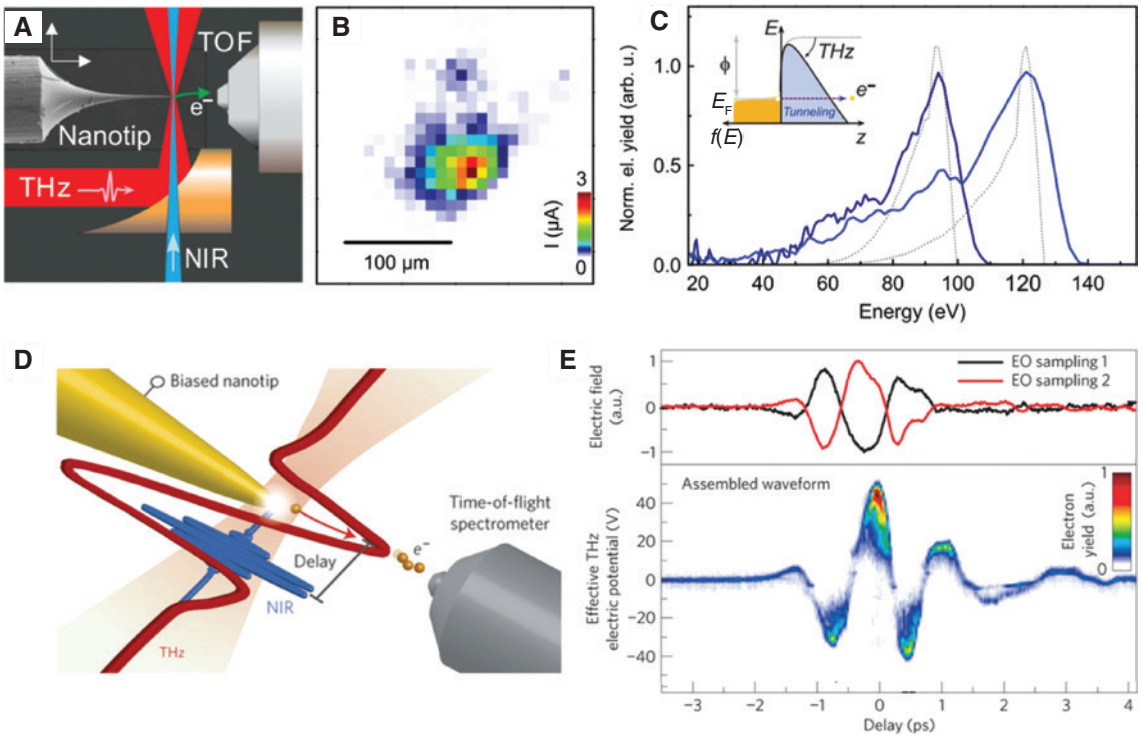

Figure 6: Nanotip-based terahertz field–driven electron emission.
(A) Schematic of terahertz field–driven electron emission experiment. Incident terahertz pulse couples to a sharp tungsten tip (tip diameter of 10 nm), and the emitted electrons are detected by a TOF electron spectrometer (3-mm distance between tip apex and entrance aperture) in a high-vacuum chamber (10^{-8} mbar range). (B) Field emission map measured by scanning the tip. (C) Electron energy spectra for two terahertz field strengths of 3.1 V/nm (black) and 5.3 V/nm (blue), revealing peaked energy distribution with sharp cutoffs. After tunneling process, the emitted electrons are accelerated by the strongly enhanced terahertz electric field. The dashed lines are numerical simulated results. (D) Terahertz control of photoemission in a pump–probe scheme in which near-infrared pulse induces photoelectrons, which are accelerated in the momentary terahertz potential. (E) Waveforms of terahertz electric field measured by electro-optic sampling (top) and terahertz streaking spectroscopy of nanotip photoemission (bottom). The figures (A–C) and (D, E) are reproduced from References [47] and [65], respectively.

energy spacing, charging energies, and so on [50, 51]. To couple the terahertz waves to a single molecule trapped between nanogap electrodes, however, it is inevitable to utilize the plasmonic effects of metal electrodes with a nanometer sized gap.

Bowtie-shaped antenna for the source and drain electrode can be employed for single-molecule transistors to achieve a good coupling efficiency between the terahertz waves and the tunneling electrons. By using the plasmonic effect, furthermore, the terahertz field in the gap is enhanced by a factor of ~10^5 in a nanometric volume, enabling strong terahertz field–induced nonlinear response such as photon-assisted tunneling and two-photon absorption [50, 67]. As shown in Figure 7A–C, it was reported that the strong terahertz fields can create additional electron tunneling pathways in a single-molecule transistor in which a bowtie-shaped metal antenna plays a role as a metal electrode. Experimentally, the additional lines parallel to the ground-state lines in Coulomb stability diagrams were observed in the single-electron transport and Coulomb blockaded regions (Figure 7C). The observed energy separations ~10 meV (middle) corresponding to the photon energy of the incident terahertz waves indicate resonant terahertz-assisted tunneling effect (middle of Figure 7C), and the data for the higher terahertz irradiation show that two-photon absorption takes place (right of Figure 7C). Furthermore, a recent work demonstrated low-energy excitation in single fullerene molecules transistor by vibron-assisted tunneling promoted by the terahertz-induced oscillation of the molecule (Figure 7D) [82]. The vibrational modes of molecule (~2 and ~4 meV) [83] create new tunneling paths for electrons observed in terahertz-induced photocurrent measured by using the time-domain terahertz autocorrelation measurement combined with bowtie antenna-based single-molecule transistor geometry (Figure 7E, F).

3.2.2 Terahertz field emission

As shown in Figure 8A, the locally enhanced terahertz electric field in the gap of a dipole antenna contributes to

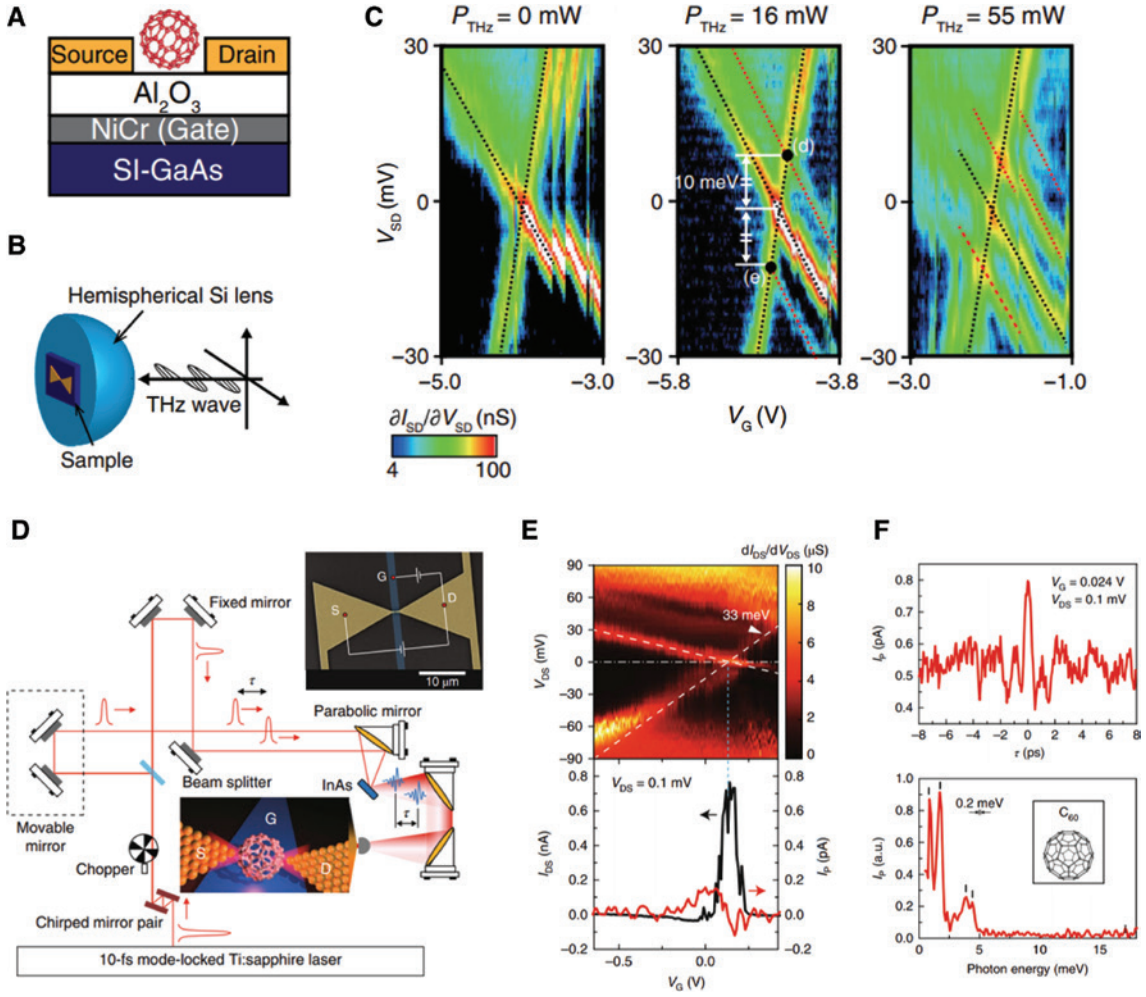

Figure 7: Photon-assisted tunneling in single-molecule transistors based on a bowtie antenna.
(A, B) Schematic of cross-sectional view for a single-molecule transistor where a fullerene molecule is trapped in a bowtie antenna and the sample mounted on a hemispherical silicon lens, respectively. (C) Coulomb stability diagrams under the terahertz irradiation with three different powers [0 mW (left), 16 mW (middle), and 55 mW (right)] and a fixed frequency (2.5 THz). (D) Setup for single molecule terahertz spectroscopy based on terahertz autocorrelation system. (E) Coulomb stability diagrams (top), the single electron tunneling current (black), and the terahertz-induced photocurrent (red) as a function of gate voltage at a source-drain voltage of 0.1 mV (bottom) for C_{60} single-molecule transistor. (F) Quasi-autocorrelation trace of the terahertz-induced photocurrent and its Fourier spectrum. The figures (A–C) and (D–F) are reproduced from References [50] and [82], respectively.

electric field emission into vacuum. The resonant excitation of the dipole antenna by an intense terahertz pulse of ~100 kV/cm enables the field strength in the dipole gap to reach up to ~10 MV/cm, which requires a field enhancement factor of ~100 (Figure 8B, C). The dipole antennas for the terahertz field–driven field emission experiment are fabricated on a thin SiNx film, and then the SiNx substrate in the vicinity of the gap is selectively etched away (Figure 8D, F). This allows the motion of free electrons emitted across the gap. Figure 8D–G show scanning electron microscopy (SEM) images of dipole antenna with a capacitive gap of around 2 μm before and after terahertz exposure for 1 h. In the vicinity of the gap, the gold has moved inward with reducing the gap to around 1 μm. The gold deformation occurring near the gap of dipole antennas results from electromigration due to high-energy field–emitted electrons. The mass transfer of gold produces current channel across the gap; therefore, the spectral change of dipole antennas by strong terahertz field irradiation can be modeled by a decrease in resistivity between the antennas (Figure 8H).

3.3 Metal nanoslit and slot antenna

3.3.1 Terahertz nonlinear transmission response

The vertically aligned metallic nanogaps can initiate the terahertz nonlinear response arising from the quantum tunneling effect. Noble metals such as gold or copper are

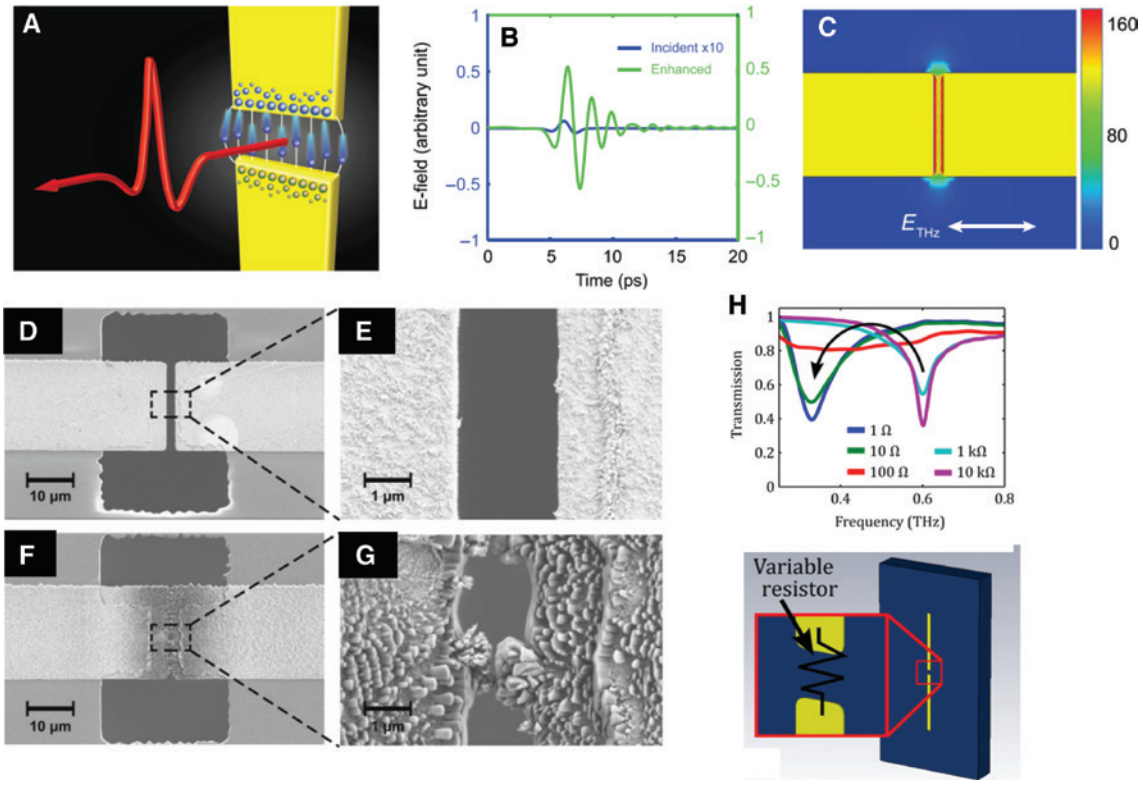

Figure 8: Dipole antenna-based terahertz field–driven electron emission.
(A) Illustration of terahertz-induced field emission experiment. The single-cycle strong terahertz pulse enables electrons escape from the gold–vacuum interface. (B) Resonantly enhanced terahertz field in time domain at the gap of dipole antenna. (C) Simulated result of two-dimensional spatial distribution of electric field enhancement. (D–G) SEM images of a dipole antenna gap before (D, E) and after (F, G) strong terahertz field exposure. (H) Transmission spectra for five different resistances identified in the dipole antenna gap. The figures (A–G) and (H) are reproduced from References [27] and [84], respectively.

good conductors in terahertz frequencies; therefore, they can induce extremely large field enhancement enough to reach the quantum regime with the few nanometer-sized gap structures [85]. Figure 9A shows the experimental scheme for the terahertz quantum plasmonics using intense terahertz pulse [86, 87] and metallic nanogap structures [14]. Here, nanogaps are fabricated with the gap sizes of 5 and 1.5 nm by Al_2O_3 layers sandwiched by gold film, and copper single-layer graphene–copper for extreme terahertz field enhancement [33]. Figure 9B presents transmitted amplitudes through a 1.5-nm gap resonant ring antenna for different incident terahertz field strengths, which are normalized by the maximum field amplitudes passing through a bare quartz substrate. As the incident field approaches 150 kV/cm, the transmitted field is considerably reduced by the terahertz field–induced tunneling across the nanogaps. Figure 9C shows the temporally integrated transmittance ($T \equiv \int E_{sample}{}^2(t)\,dt / \int E_{reference}{}^2(t)dt$, where E_{sample} is field amplitude through the nanogap sample and $E_{reference}$ is the field amplitude though the bare substrate), which is normalized by the transmittance T_0 of the minimum incident field strength. The transmittance value eventually reduces by 50% as the field inside the gap E_{gap} increases to 5 V/nm. It is worth to note that the similar field strength of V/nm in static field regime can damage the gap [88].

By pushing the limit of the gap size reducing down to the single atomic scale, we can pursue to a dramatic terahertz nonlinear response from the nanogap structures. The bottom image of Figure 9A shows the extreme, a metallic nanogap separated by a single-layer graphene, which is made by recently developed lithography method [13]. These gaps with a single layer of carbon atoms in the middle have been approximated by a single 3-angstrom-wide gap with a dielectric constant of three [89, 90], across which strong quantum tunneling may occur [91–93]. Figure 9D shows measured time traces of terahertz field amplitudes transmitted through the sample for various incident terahertz pulse strengths, normalized by the maximum field amplitudes transmitted through the quartz substrate only. By increasing the incident terahertz electric field up to $E_{0,max}$ ~192 kV/cm, the normalized transmitted amplitude in the time domain dramatically decreases, down to 0.16% at the maximum. This gives rise to a 97% reduction

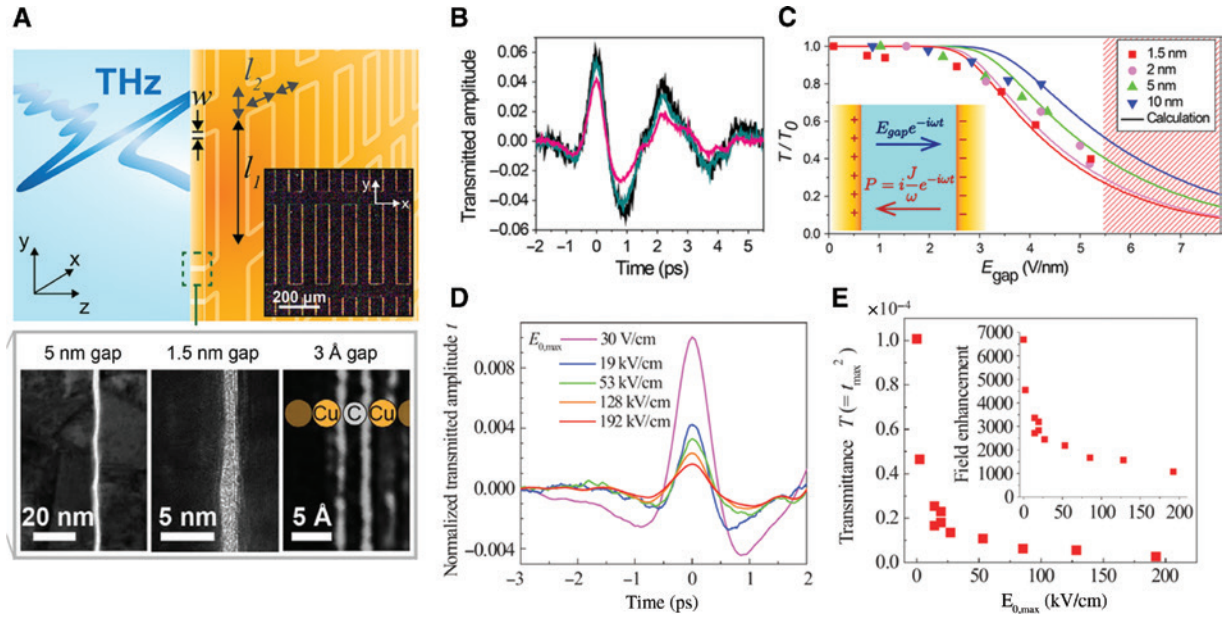

Figure 9: Terahertz funneling-induced electron tunneling in metal gaps.
(A) Terahertz pulse is passing through a metallic nanogap structure. At the bottom figure, cross-sectional transmission electron microscopy (TEM) images for nanogaps are shown; 5- and 1.5-nm gaps composed of alumina layer sandwiched by gold and 3-angstrom gap composed of a single-layer graphene sandwiched by coppers. (B) Measured amplitudes of transmitted terahertz pulses through the 1.5-nm alumina gap as a function of incident terahertz field strengths (black: 20 kV/cm, green: 75 kV/cm and red: 150 kV/cm). (C) Measured (dots) and calculated (lines) terahertz transmittance normalized by minimum transmittance value as a function of field strength inside the gap for different alumina layer thicknesses. Dashed region indicates that nanogaps are damaged after the measurement when the corresponding field strength is applied at the gap. (D) Measured amplitudes of transmitted terahertz pulses through the copper–graphene–copper gap as a function of incident terahertz field strengths. (E) Absolute terahertz transmittance as a function of field amplitude inside the graphene gap. Inset shows terahertz field enhancement factors as a function of incident field strength. The figures (A–C) and (D, E) are reproduced from References [13] and [14], respectively.

in normalized transmitted power. Figure 9E shows the normalized transmittance T and field enhancement factor (inset) at the maximum in time domain, as a function of the strength of the incident terahertz electric field.

When the applied electric field is sufficiently strong to flow tunneling current across the gap, the effective refractive index of the gap medium becomes larger, which in turn limits the field enhancement [93, 94]. This self-limited transmission by quantum tunneling can be observed without damaging the gaps by using a single-cycle terahertz pulse (~1 ps) [21, 95]. On the other hand, it is not easy to observe the nonlinear transmission by using optical pulses [16]. This trend is summarized in Figure 10. It shows transmitted peak power vs. incident power for both terahertz and near-infrared frequencies. As we can see, the terahertz nonlinearities are obvious for both structures. As the incident power increases, the transmitted power deviates further away from the linear regime (dashed line) due to the quantum tunneling induced by the terahertz field. On the contrary, nonlinearity is hardly seen in the near-infrared regime for both nanogap samples. Before reaching the nonlinear transmission regime, the sample is damaged in the near-infrared. This behavior can be explained by estimating tunneling conductivity and displacement conductivity in both frequency ranges. The results indicate that the tunneling conductivity σ_t is the same for terahertz and near-infrared frequencies for the same field strength, while the frequency-dependent displacement conductivity ($\sigma_d = -i\omega\epsilon_0\epsilon_{gap}$) takes relatively large portion compared to the tunneling conductivity in the near-infrared [16]. As a result, tunneling-induced transmission modulation is negligible in the near-infrared.

3.3.2 Terahertz tunneling transport

The nanogap structure in configuration of a metallic slit, composed of optically thick metal films extended far for many wavelengths in lateral direction and optically transparent insulating layer sandwiched between the metals, can be modeled by an equivalent circuit with appropriate parameters [96, 97] as shown in Figure 11A. Here, the fields of the incident and transmitted light coincide with the applied current and voltage that are studied in impedance measurements. When an electromagnetic wave has its magnetic field aligned parallel to the slit (TM polarization), a current $I_0(t)$ is induced in the metal, which flows toward the gap. For normally incident plane

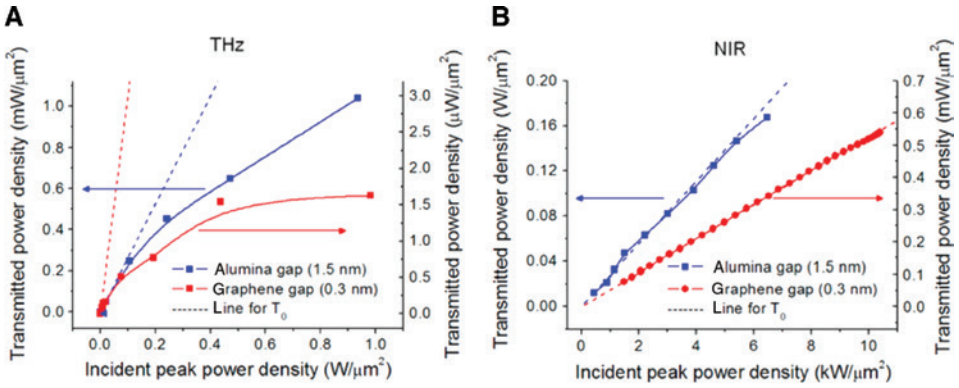

Figure 10: Transmission nonlinearity by electron tunneling in metal gaps.
Transmitted peak power densities for 1.5-nm alumina gap and 0.3-nm graphene gap samples as a function of incident peak power densities in frequency of (A) terahertz ($\lambda \sim 750$ μm) and (B) near IR ($\lambda \sim 830$ nm). Dots indicate the measured values, and dotted lines mean linear regime without tunneling effect. The figures are reproduced from Reference [16].

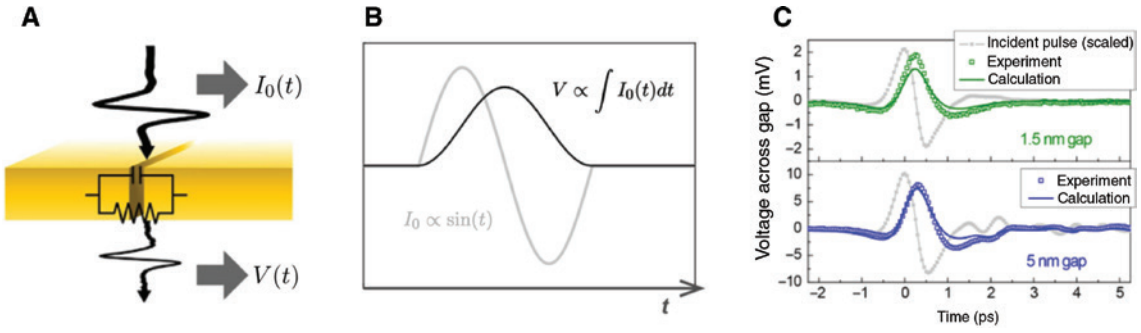

Figure 11: Terahertz tunneling transport in metal nanogaps.
(A) Illustration of terahertz transmission through a metallic slit by equivalent circuit model. Incident terahertz field is represented by current source I_0, and the transmitted field corresponds to the voltage across the gap V. Characteristic capacitance C and resistance R are assigned to the nanogap structure. (B) General phase relation between the applied current source I_0 and resulting voltage across the gap V of a capacitor. (C) Measured voltage time trace across the gap, whose gap width of 1.5 or 5 nm was estimated from the terahertz transmission measurement through the metallic slit structure. The shapes of the incident terahertz pulse time traces are shown as gray curves. The figures are reproduced from Reference [96].

waves, the current is expressed in terms of an effective surface current density $\mathbf{K}_0 = \mathbf{n} \times (2\mathbf{H}_{inc})$, where $\mathbf{n}$ is the unit vector normal to the metal surface and $\mathbf{H}_{inc}$ is the magnetic field vector of the incident wave. Therefore, the current I_0 can be expressed with the incident field $\mathbf{H}_{inc}$ by the relation $I_0 = |\mathbf{K}_0| \times l$ with slit length scale l, which corresponds to the beam spot size illuminating the sample. The voltage across the gap $V(t)$ simply equals the width of the gap times the (enhanced) electric field strength inside the gap. As derived from the Kirchhoff integral formalism [26, 98–100], the near-field enhancement is directly proportional to the transmitted field determined in the far field. In short, evaluating the incident and transmitted fields allows for a direct measure of the applied current and induced voltage at the gap, respectively. For a narrow slit, whose width is much narrower than the metal thickness, a capacitor-like behavior is expected [26, 97]. Then, the voltage across gap $V(t)$ is connected to the applied current $I_0(t)$ by the relation $V(t) = (\int I_0(t)\, dt)/C$, where C is the capacitance of the nanogap structure. In particular, if we consider a harmonic time dependence, given by $e^{-i\omega t}$, the equation is rewritten as $V = I_0/(-i\omega C)$ in the frequency domain. This is illustrated in Figure 11B by the phase lag of $\pi/2$ between the induced voltage and the applied current. The great advantage of the circuit model analysis is on the ability to provide quantitative agreement with the experimental results without any fitting parameters but by considering only the amplitude profile of the incident pulse and the dimensions of the capacitor (such as the gap size, metal thickness, and refractive index of the insulating layer), which are known prior to the measurements. For example, Figure 11C shows the terahertz transmission through a slit

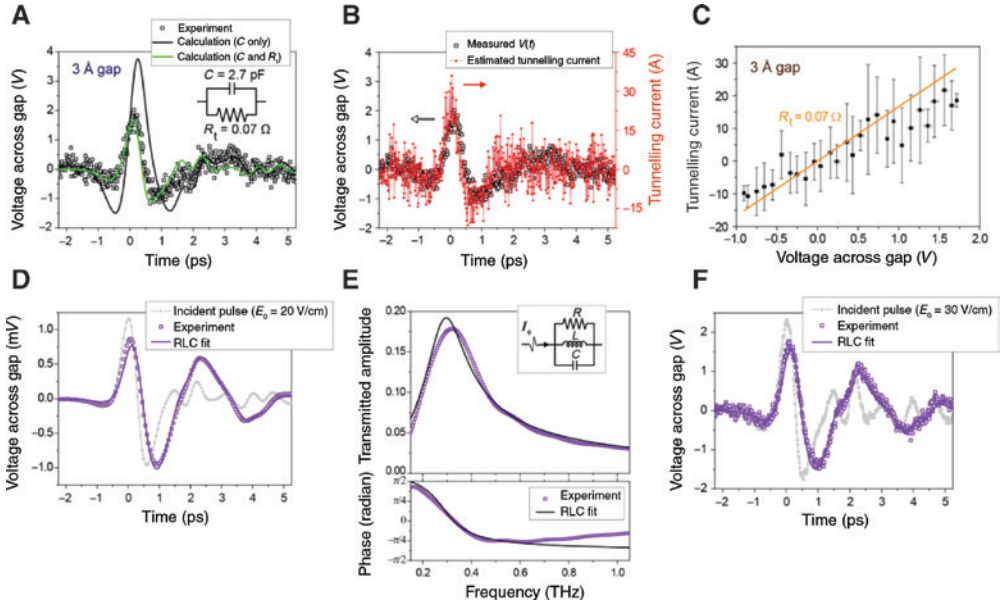

Figure 12: Terahertz tunneling transport in metal angstromgaps.
(A) Measured voltage time trance through a 3-angstrom–sized metal–graphene–metal gap at an incident field strength of 30 kV/cm. The inset shows the equivalent circuit of the gap. (B) Measured voltage across the gap $V(t)$, which is identical to the experimental data in (A), and the extracted tunneling current. An unweighted sliding-average smooth of 11 data points is applied to the tunneling current to produce a less noisy temporal amplitude profile. (C) An *I-V* plot obtained from the results of (B) and a line that represents a tunneling resistance R_t of 0.07 Ω. (D, E) Temporal profile of the voltage across the alumina gap and the corresponding Fourier-transformed amplitude and phase of terahertz waves transmitted through the nanoslot array at an incident field strength of 20 V/cm. The inset in (E) shows the equivalent circuit of the nanoslot array. (F) Transmission through the same sample by a terahertz pulse with a field strength of 30 kV/cm. The figures are reproduced from Reference [96].

that has gap widths of 1.5 and 5 nm and compared with the circuit modeling results.

As we have seen, the nonlinear effect can alter the terahertz transmission by the tunneling electrons across the gap, and the above simple capacitor picture for the slit structure may not be applied to the nonlinear response [94]. It could be necessary to modify the optical properties of the insulating medium by including additional parameters such as resistance R. When intense terahertz pulse (peak value of $E_0 = 30$ kV/cm) is incident on a nanogap whose gap dimension is only a few angstroms, a maximum of 2 V is induced across the atomic gap, as indicated in Figure 12A. Determined from the structural dimensions of the gap and an effective permittivity ε_{gap} of 3 [13, 89, 90], a capacitance of $C = 2.7$ pF alone fails to correctly describe the features of the transmitted terahertz wave in this case. Electron tunneling through the gap prevents charge accumulation at the metal edges and causes a reduced voltage across the gap, and the shape of the transmitted pulse closely resembles the profile of the single-cycle incident pulse. Thus, a finite tunneling resistance R_t connected in parallel to the innate slit capacitance should be added to the total impedance, which relates the transient voltage to the current applied by the incident radiation [14]. If a constant tunneling resistance is assumed over the studied voltage range, a value of 0.07 Ω offers a good fit to the experimental results. On the other hand, the circuit model is able to provide a differential equation that links the measured applied current $I_0(t)$ and induced voltage $V(t)$, and the tunneling resistance can be deduced without assuming that the resistance value is fixed; the tunneling current $I_0(t) - C\,dV/dt$ is obtained from the source current $I_0(t)$ and measured voltage across the gap $V(t)$. The extracted tunneling current shown in Figure 12B is proportional to the voltage across the gap $V(t)$, suggesting an ohmic response of the tunneling electrons through the gap. Figure 12C is a current–voltage characteristic obtained from the mean value of the data points within every 0.1-V interval of the voltage across the gap; error bars indicate the standard deviation. The plot agrees with the slope of 0.07 Ω that was evaluated from the fit in Figure 12A.

Because the tunneling resistance and the capacitance C of the slit form a parallel circuit, the resistance being measured should be comparable to the impedance $Z = 1/(-i\omega C)$ or smaller to be detectable. Therefore, the factor $1/|Z|$ specifies the resolution of the circuit analysis when measuring the tunneling current. Smaller tunneling currents are measurable if the slit capacitance is decreased; presumably, the most efficient way to achieve this in the slit structure is to shorten the slit length l so that the slit reduces to a close-ended slot. Additionally, transmission of

electromagnetic waves becomes challenging, as extremely narrow gaps are required to observe quantum effects. Resonance structures, such as slot antennas, allow an increase in transmittance for certain bandwidths, which can also be improved for broadband purposes using multiresonance structures [101], and exhibit a better signal-to-noise ratio than slits that suffer from a capacitor-like broad $1/f$-type spectral response. Figure 12D and E show the time trace of the voltage across the gap and its Fourier analysis through ring-shaped slot antenna whose resonance is placed near 0.3 THz for an incident pulse strength of $E_0 = 20$ V/cm. For this case, the circuit analysis is also possible to describe the terahertz response by an RLC (a resistor (R), an inductor (L), and a capacitor (C)) circuit [102], as depicted in the inset of Figure 12D. The parameters R, L, and C are determined from the complex impedance for a parallel RLC circuit to acquire the best fit with the transmitted pulse $V(t)$ from the measured incident pulse $I_0(t)$. Moreover, a phase parameter θ is introduced to compensate for an additional phase shift in the transmitted wave due to coupling effects between nearby antennas, which is predicted from calculations based on modal expansion [103]. Accordingly, an equivalent waveform is reproduced in Figure 12D by using the equation $V = \frac{1}{\frac{1}{R} - \frac{1}{i\omega L} - i\omega C} I_0 e^{i\theta}$ together with the values of $R = 5.83\ \Omega$, $L = 1.72 \times 10^{-12}$ H, $C = 1.69 \times 10^{-13}$ F, and $\theta = 20.6°$. These four parameters are essential to fit the amplitude of the resonance peak, the resonant frequency, the line width, and the phase in the frequency domain. The same procedure is carried out for an incident pulse of $E_0 = 30$ kV/cm. For such moderate intensities, where quantum effects are negligible, the same values of the four parameters also thoroughly duplicate the experimental data, as shown in Figure 12E.

3.3.3 Terahertz tunneling rectification

Figure 13A shows the strategy for the terahertz tunneling rectification by using lateral, ring-shaped tunneling barriers, encasing a metallic island that is surrounded by a metallic plane [104]. By adjoining the one-dimensional tunneling junctions in two dimensions with triangle shape [33], the tunneling current flowing across the quantum barriers is determined not only by the phase of the external electromagnetic pulse [20, 105, 106], but also by the geometry of the barrier (i.e. lateral symmetry of the ring). Using the proposed method, it is possible to control the ultrafast tunneling process additionally by modifying the lateral shape of the ring and by simply changing the polarization of incoming pulses. The time-integrated total tunneling currents through the barriers are measured directly by attaching electrical probes on the sample surface as shown in Figure 13D. A THz polarizer is placed to control the direction of the surface current **K**. Figure 13E shows measured tunneling rectification currents across triangular (side length of 70 μm and perimeter of 210 μm shown in Figure 13B, C) and square (side length of 25 μm and perimeter of 100 μm) nanogap rings (gap size of 2 nm) as a function of the terahertz polarizer angle, i.e. changing incident terahertz polarization. The results show strikingly different behaviors as mentioned above. The asymmetric potential distribution along the equilateral triangle results in a net tunneling current through the contour, while the potential distribution at any point of a square is mostly counterbalanced by its corresponding point across the center, independent of the polarization of the incident pulse. Therefore, the triangle shape barrier can be used to accumulate more tunneling charges inside the metallic island under a single terahertz pulse excitation than the rectangle one, which enhances directly the experimental signal. Figure 13F displays polar plots of the tunneling currents for the triangular and square geometries. As expected, the total current vs. polarization angle shows the threefold rotational symmetry of an equilateral triangle.

Sending a femtosecond optical pulse with the terahertz pulse can provide another control parameter for the ultrafast modulation of the tunneling current. As shown in Figure 13G, the electric fields of the femtosecond optical pulse can be focused to a specific position in the ring and summed with picosecond terahertz electric fields. The optical pulse rapidly distorts the local potential barrier under the quasi-constant terahertz field, generating an additional, local tunneling current. The optically driven current is sensitively affected by the terahertz field strength at the specific position on the barrier and by the time delay between the terahertz and optical pulses, thus providing a way to visualize the spatiotemporal dynamics of the terahertz potential across the barriers. An interesting aspect of the optically modulated quantum barriers is the position-dependent ultrafast optical gating, as illustrated in Figure 13H.

Using the ring-shaped barriers and the time-resolved detection method of terahertz tunneling current by the optical pulse, terahertz full-wave rectification can be achieved, as shown in Figure 13I. Here, the spot size of the optical beam is expanded to cover the entire ring, which makes it possible to probe the total terahertz current response through the ring. Additionally, a DC bias is applied to generate a unidirectional (i.e. into or out of the loop) terahertz current across the ring barrier independent of the polarity of the incident terahertz pulse. As a result,

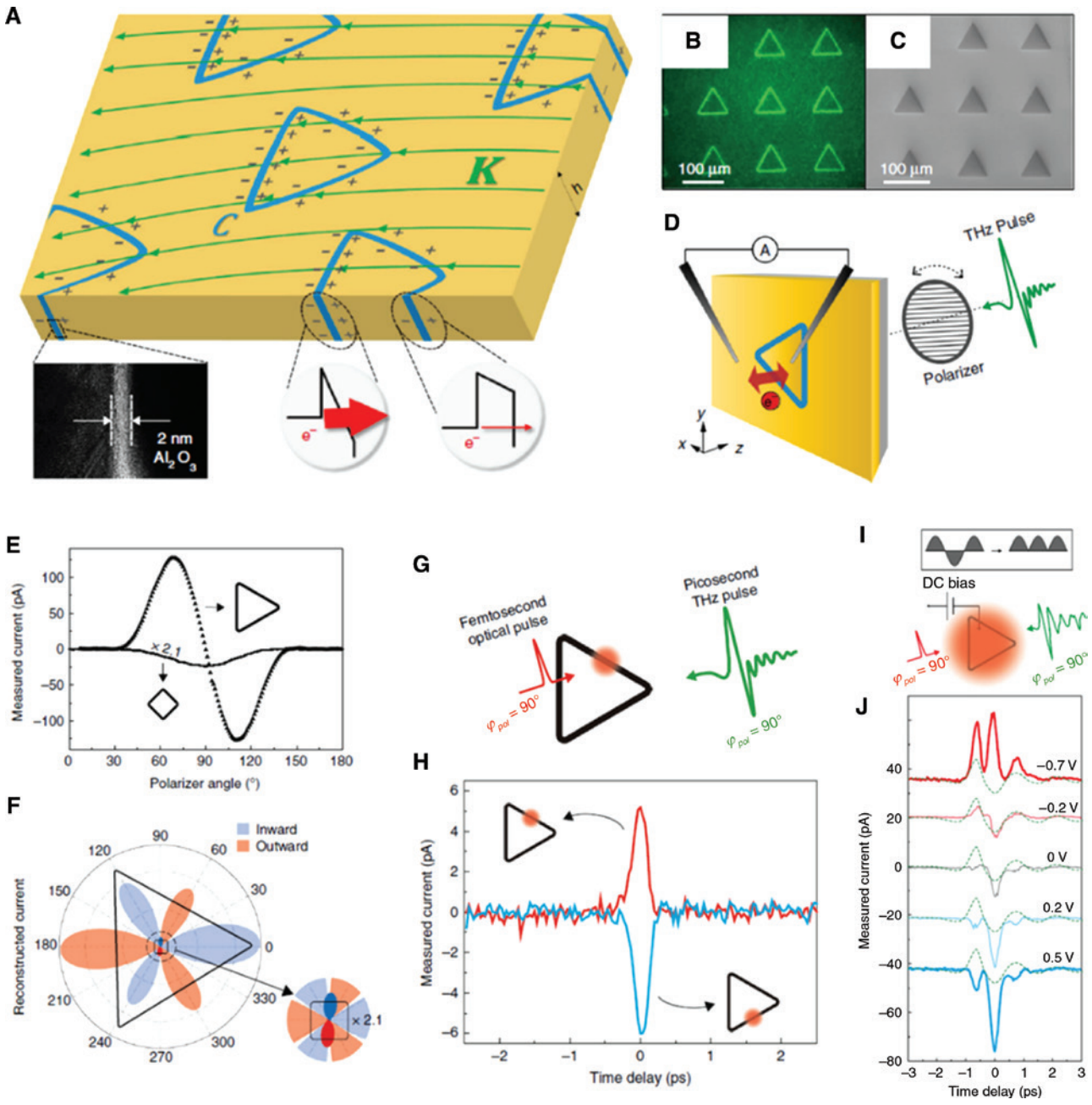

Figure 13: Terahertz tunneling rectification in metal nanogaps.
(A) Terahertz-pulse–driven tunneling current rectification using a ring-shaped nanogap sample fabricated in a metallic film. Incident terahertz field induces surface current on a metallic film (denoted by a vector field **K**), which applies terahertz electric potential across the ring-shaped tunneling barriers (denoted by contour *C*). The shape of the ring is critical for the terahertz tunneling rectification, which affects directly to the accumulation of finite electrons inside the metallic island under a terahertz pulse excitation. A TEM picture shows the cross-sectional image of the barrier, which is composed of 2-nm-thick Al_2O_3 layer sandwiched in the gold film. (B) An optical microscope image and (C) SEM image of the sample. (D) Experimental scheme. The incident THz field is linearly polarized and induces eddy current on the gold surface, which acts as a current source K both inside and outside the triangle as shown in (A). (E) Measured tunneling current as a function of incident terahertz polarization. Triangle- and rectangle-shaped barriers are exploited, which possess different symmetry properties. (F) Polar plots of the data (E). (G) Ultrafast tunneling current measurement scheme using femtosecond optical pulse illumination on the ring-shaped barriers. (H) Depending on the excitation position and time delay between the terahertz and optical pulses, the optical pulse generates position-sensitive and time-dependent switching signal. (I) Schematic of THz full-wave rectification. A DC bias imposes potential difference for the whole ring, thereby giving a preferred current direction. The optical spot is expanded to probe the total tunneling current flowing through the whole ring. (J) Measured terahertz full-wave rectification. Dashed green curves show the terahertz potential profile. The value of the applied DC bias is denoted for each curve, and the curves are vertically displaced for clarity. The figures are reproduced from Reference [104].

the terahertz wave generates a fully rectified terahertz tunneling current depending on the DC bias strength, and this transient is visualized by the optical pulse (Figure 13J).

4 Discussions and outlook

In this review, we surveyed recent works concerning terahertz control of electrons using various metallic nanostructures. The intense terahertz pulses can manipulate tunneling electrons by ultrafast modification of the potential barriers in metal nano- and subnano-junctions. Here, three different metal nanostructures utilized for terahertz-induced quantum tunneling phenomena have been discussed: metal nanotip, nanoantenna, nanoslit, and slot antenna. The first one, terahertz-coupled metal nanotip, provides atomic scale imaging and picosecond time resolution in combination with STM system and can generate localized high-energy electron bursts. The second structure, dipole antenna system with various shapes, enables terahertz-assisted single-electron tunneling based on the resonant vibrational excitation of molecule, which is trapped inside the tips. In the case of metal nanoslit and slot antennas, terahertz-induced voltage and tunneling current can be extracted experimentally with a subpicosecond time resolution, leading to quantitative analysis of tunneling currents. Further developments of terahertz quantum plasmonics in terms of tunneling electron manipulation will require improvement of spatiotemporal resolutions and advances in the generation and detection of terahertz pulses, as well as easy-to-implement subatomic scale distance controls. Beyond terahertz field–driven electron tunneling, the coherent tunneling currents can be controlled by a few femtosecond phase–locked driving pulses using a single cycle of mid and near-infrared light.

Acknowledgments: This work was supported by the National Research Foundation of Korea (NRF) grant funded by the Korean government (MSIP: NRF-2015R1A3A2031768, Funder Id: http://dx.doi.org/10.13039/501100001321, NRF-2019R1G1A1007912) (MOE: BK21 Plus Program 21A20131111123, Funder Id: http://dx.doi.org/10.13039/501100001321) and the 2019 Research Fund of UNIST.

References

[1] Hirori H, Doi A, Blanchard F, Tanaka K. Single-cycle terahertz pulses with amplitudes exceeding 1 MV/cm generated by optical rectification in $LiNbO_3$. Appl Phys Lett 2011;98:091106.

[2] Reimann K, Smith RP, Weiner AM, Elsaesser T, Woerner M. Direct field-resolved detection of terahertz transients with amplitudes of megavolts per centimeter. Opt Lett 2003;28:471–3.

[3] Hebling J, Yeh K-L, Hoffmann MC, Bartal B, Nelson KA. Generation of high-power terahertz pulses by tilted-pulse-front excitation and their application possibilities. J Opt Soc Am B 2008;25:B6–19.

[4] Kim KY, Taylor AJ, Glownia JH, Rodriguez G. Coherent control of terahertz supercontinuum generation in ultrafast laser–gas interactions. Nat Photon 2008;2:605–9.

[5] Sell A, Leitenstorfer A, Huber R. Phase-locked generation and field-resolved detection of widely tunable terahertz pulses with amplitudes exceeding 100 MV/cm. Opt Lett 2008;33:2767–9.

[6] Hwang HY, Fleischer S, Brandt NC, et al. A review of non-linear terahertz spectroscopy with ultrashort tabletop-laser pulses. J Mod Opt 2015;62:1447–79.

[7] Luo CW, Reimann K, Woerner M, Elsaesser T, Hey R, Ploog KH. Phase-resolved nonlinear response of a two-dimensional electron gas under femtosecond intersubband excitation. Phys Rev Lett 2004;92:047402.

[8] Fleischer S, Zhou Y, Field RW, Nelson KA. Molecular orientation and alignment by intense single-cycle THz pulses. Phys Rev Lett 2011;107:163603.

[9] Yamaguchi K, Nakajima M, Suemoto T. Coherent control of spin precession motion with impulsive magnetic fields of half-cycle terahertz radiation. Phys Rev Lett 2010;105:237201.

[10] Kampfrath T, Sell A, Klatt G, et al. Coherent terahertz control of antiferromagnetic spin waves. Nat Photon 2011;5:31–4.

[11] Katayama I, Aoki H, Takeda J, et al. Ferroelectric soft mode in a $SrTiO_3$ thin film impulsively driven to the anharmonic regime using intense picosecond terahertz pulses. Phys Rev Lett 2012;108:097401.

[12] Somma C, Reimann K, Flytzanis C, Elsaesser T, Woerner M. High-field terahertz bulk photovoltaic effect in lithium niobate. Phys Rev Lett 2014;112:146602.

[13] Bahk Y-M, Kang BJ, Kim YS, et al. Electromagnetic saturation of angstrom-sized quantum barriers at terahertz frequencies. Phys Rev Lett 2015;115:125501.

[14] Kim J-Y, Kang BJ, Park J, et al. Terahertz quantum plasmonics of nanoslot antennas in nonlinear regime. Nano Lett 2015;15:6683–8.

[15] Cocker TL, Peller D, Yu P, Repp J, Huber R. Tracking the ultrafast motion of a single molecule by femtosecond orbital imaging. Nature 2016;539:263–7.

[16] Han S, Kim J-Y, Kang T, et al. Colossal terahertz nonlinearity in angstrom- and nanometer-sized gaps. ACS Photon 2016;3:1440–5.

[17] Jelic V, Iwaszczuk K, Nguyen PH, et al. Ultrafast terahertz control of extreme tunnel currents through single atoms on a silicon surface. Nat Phys 2017;13:591–8.

[18] von Hoegen A, Mankowsky R, Fechner M, Först M, Cavalleri A. Probing the interatomic potential of solids with strong-field nonlinear phononics. Nature 2018;555:79–82.

[19] Cocker TL, Jelic V, Gupta M, et al. An ultrafast terahertz scanning tunnelling microscope. Nat Photon 2013;7:620–5.

[20] Yoshioka K, Katayama I, Minami Y, et al. Real-space coherent manipulation of electrons in a single tunnel junction by single-cycle terahertz electric fields. Nat Photon 2016;10:762–5.

[21] Schubert O, Hohenleutner M, Langer F, et al. Sub-cycle control of terahertz high-harmonic generation by dynamical Bloch oscillations. Nat Photon 2014;8:119–23.
[22] Hafez HA, Kovalev S, Deinert JC, et al. Extremely efficient terahertz high-harmonic generation in graphene by hot Dirac fermions. Nature 2018;561:507–11.
[23] Yoshioka K, Minami Y, Shudo K, et al. Terahertz-field–induced nonlinear electron delocalization in Au nanostructures. Nano Lett 2015;15:1036–40.
[24] Pendry JB, Martín-Moreno L, Garcia-Vidal FJ. Mimicking surface plasmons with structured surfaces. Science 2004;305:847–8.
[25] Tarekegne AT, Iwaszczuk K, Zalkovskij M, Strikwerda AC, Jepsen PU. Impact ionization in high resistivity silicon induced by an intense terahertz field enhanced by an antenna array. New J Phys 2015;17:043002.
[26] Seo MA, Park H, Koo S, et al. Terahertz field enhancement by a metallic nano slit operating beyond the skin-depth limit. Nat Photon 2009;3:152–6.
[27] Strikwerda AC, Zalkovskij M, Iwaszczuk K, Lorenzen DL, Jepsen PU. Permanently reconfigured metamaterials due to terahertz induced mass transfer of gold. Opt Express 2015;23:11586–99.
[28] Keiser GR, Seren HR, Strikwerda AC, Zhang X, Averitt RD. Structural control of metamaterial oscillator strength and electric field enhancement at terahertz frequencies. Appl Phys Lett 2014;105:081112.
[29] Lange C, Maag T, Hohenleutner M, et al. Extremely nonperturbative nonlinearities in GaAs driven by atomically strong terahertz fields in gold metamaterials. Phys Rev Lett 2014;113:227401.
[30] Park H-R, Ahn KJ, Han S, Bahk YM, Park N, Kim DS. Colossal absorption of molecules inside single terahertz nanoantennas. Nano Lett 2013;13:1782–6.
[31] Choi G, Bahk YM, Kang T, et al. Terahertz nanoprobing of semiconductor surface dynamics. Nano Lett 2017;17:6397–401.
[32] Mittleman DM. Frontiers in terahertz sources and plasmonics. Nat Photon 2013;7:666–9.
[33] Chen X, Park HR, Pelton M, et al. Atomic layer lithography of wafer-scale nanogap arrays for extreme confinement of electromagnetic waves. Nat Commun 2013;4:2361.
[34] Liu G, He M, Tian Z, Li J, Liu J. Terahertz surface plasmon sensor for distinguishing gasolines. Appl Opt 2013;52:5695–700.
[35] Park SJ, Hong JT, Choi SJ, et al. Detection of microorganisms using terahertz metamaterials. Sci Rep 2014;4:4988.
[36] Singh R, Cao W, Al-Naib I, Cong L, Withayachumnankul W, Zhang W. Ultrasensitive terahertz sensing with high-Q Fano resonances in metasurfaces. Appl Phys Lett 2014;105:171101.
[37] Jeong J, Yun HS, Kim D, et al. High contrast detection of water-filled terahertz nanotrenches. Adv Opt Mater 2018;6:1800582.
[38] Choi SB, Kyoung JS, Kim HS, et al. Nanopattern enabled terahertz all-optical switching on vanadium dioxide thin film. Appl Phys Lett 2011;98:071105.
[39] Lee SH, Choi M, Kim TT, et al. Switching terahertz waves with gate-controlled active graphene metamaterials. Nat Mater 2012;11:936–41.
[40] Shen N-H, Massaouti M, Gokkavas M, et al. Optically implemented broadband blueshift switch in the terahertz regime. Phys Rev Lett 2011;106:037403.
[41] Chen H-T, Padilla WJ, Zide JMO, et al. Ultrafast optical switching of terahertz metamaterials fabricated on ErAs/GaAs nanoisland superlattices. Opt Lett 2007;32:1620–2.
[42] Kyoung J, Jang EY, Lima MD, et al. A reel-wound carbon nanotube polarizer for terahertz frequencies. Nano Lett 2011;11:4227–31.
[43] Wu D, Fang N, Sun C, et al. Terahertz plasmonic high pass filter. Appl Phys Lett 2003;83:201–3.
[44] Lu M, Li W, Brown ER. Second-order bandpass terahertz filter achieved by multilayer complementary metamaterial structures. Opt Lett 2011;36:1071–3.
[45] Lee JW, Seo M, Park D, et al. Shape resonance omni-directional terahertz filters with near-unity transmittance. Opt Express 2006;14:1253–9.
[46] Kang J-H, Kim D-S, Seo M. Terahertz wave interaction with metallic nanostructures. Nanophotonics 2018;7:763–93.
[47] Wimmer L, Herink G, Solli DR, Yalunin SV, Echternkamp KE, Ropers C. Terahertz control of nanotip photoemission. Nat Phys 2014;10:432–6.
[48] Kim D, Jeong J, Choi G, et al. Giant field enhancements in ultrathin nanoslots above 1 terahertz. ACS Photon 2018;5:1885–90.
[49] Kim N, In S, Lee D, et al. Colossal terahertz field enhancement using split-ring resonators with a sub-10 nm gap. ACS Photon 2018;5:278–83.
[50] Yoshida K, Shibata K, Hirakawa K. Terahertz field enhancement and photon-assisted tunneling in single-molecule transistors. Phys Rev Lett 2015;115:138302.
[51] Woerner M, Somma C, Reimann K, et al. Terahertz driven amplification of coherent optical phonons in GaAs coupled to a metasurface. Phys Rev Lett 2019;122:107402.
[52] Barnes WL, Dereux A, Ebbesen TW. Surface plasmon subwavelength optics. Nature 2003;424:824–30.
[53] Kim HY, Kim DS. Selection rule engineering of forbidden transitions of a hydrogen atom near a nanogap. Nanophotonics 2018;7:229.
[54] Park H-R, Bahk YM, Choe JH, et al. Terahertz pinch harmonics enabled by single nano rods. Opt Express 2011;19:24775–81.
[55] Gramotnev DK, Bozhevolnyi SI. Plasmonics beyond the diffraction limit. Nat Photon 2010;4:83–91.
[56] Koo S, Kumar MS, Shin J, Kim D, Park N. Extraordinary magnetic field enhancement with metallic nanowire: role of surface impedance in Babinet's principle for sub-skin-depth regime. Phys Rev Lett 2009;103:263901.
[57] Kihm HW, Koo SM, Kim QH, et al. Bethe-hole polarization analyser for the magnetic vector of light. Nat Commun 2011;2:451.
[58] Jain PK, Ghosh D, Baer R, Rabani E, Alivisatos AP. Near-field manipulation of spectroscopic selection rules on the nanoscale. Proc Natl Acad Sci U S A 2012;109:8016–9.
[59] Takase M, Ajiki H, Mizumoto Y, et al. Selection-rule breakdown in plasmon-induced electronic excitation of an isolated single-walled carbon nanotube. Nat Photon 2013;7:550–4.
[60] Park W, Lee Y, Kang T, Jeong J, Kim DS. Terahertz-driven polymerization of resists in nanoantennas. Sci Rep 2018;8:7762.
[61] Lakowicz JR. Plasmonics in biology and plasmon-controlled fluorescence. Plasmonics 2006;1:5–33.
[62] Khajemiri Z, Lee D, Hamidi SM, Kim DS. Rectangular plasmonic interferometer for high sensitive glycerol sensor. Sci Rep 2019;9:1378.
[63] Yun HS, Jeong J, Kim D, Kim D-S. Active thermal control of 5 nm gap terahertz antennas. Adv Opt Mater 2019;7:1800856.
[64] Schertz F, Schmelzeisen M, Kreiter M, Elmers HJ, Schönhense G. Field emission of electrons generated by the near field of strongly coupled plasmons. Phys Rev Lett 2012;108:237602.

[65] Herink G, Wimmer L, Ropers C. Field emission at terahertz frequencies: AC-tunneling and ultrafast carrier dynamics. New J Phys 2014;16:123005.
[66] Toma A, Tuccio S, Prato M, et al. Squeezing terahertz light into nanovolumes: nanoantenna enhanced terahertz spectroscopy (NETS) of semiconductor quantum dots. Nano Lett 2015;15:386–91.
[67] Shibata K, Umeno A, Cha KM, Hirakawa K. Photon-assisted tunneling through self-assembled InAs quantum dots in the terahertz frequency range. Phys Rev Lett 2012;109:077401.
[68] Park HR, Koo SM, Suwal OK, et al. Resonance behavior of single ultrathin slot antennas on finite dielectric substrates in terahertz regime. Appl Phys Lett 2010;96:211109.
[69] Bahk Y-M, Han S, Rhie J, et al. Ultimate terahertz field enhancement of single nanoslits. Phys Rev B 2017;95:075424.
[70] Ahn JS, Kang T, Singh DK, et al. Optical field enhancement of nanometer-sized gaps at near-infrared frequencies. Opt Express 2015;23:4897–907.
[71] Kang T, Rhie J, Park J, et al. Resonance tuning of electric field enhancement of nanogaps. Appl Phys Express 2015;8:092003.
[72] Lee K, Jeong J, Bahk Y-M, et al. Microwave funneling through sub-10 nm nanogaps. ACS Photon 2016;3:537–42.
[73] Simmons JG. Generalized formula for the electric tunnel effect between similar electrodes separated by a thin insulating film. J Appl Phys 1963;34:1793–803.
[74] Simmons JG. Potential barriers and emission-limited current flow between closely spaced parallel metal electrodes. J Appl Phys 1964;35:2472–81.
[75] Fowler RH, Nordheim L. Electron emission in intense electric fields. Proc R So Lond A 1928;119:173–81.
[76] Yoshioka K, Katayama I, Arashida Y, et al. Tailoring single-cycle near field in a tunnel junction with carrier–envelope phase-controlled terahertz electric fields. Nano Lett 2018;18:5198–204.
[77] Yoshida S, Hirori H, Tachizaki T, et al. Subcycle transient scanning tunneling spectroscopy with visualization of enhanced terahertz near field. ACS Photon 2019;6:1356–64.
[78] Wang K, Mittleman DM, Van der Valk NCJ, Planken P. Antenna effects in terahertz apertureless near-field optical microscopy. Appl Phys Lett 2004;85:2715–7.
[79] Walther M, Chambers GS, Liu Z, Freeman MR, Hegmann FA. Emission and detection of terahertz pulses from a metal-tip antenna. J Opt Soc Am B 2005;22:2357–65.
[80] Wang K, Mittleman DM. Metal wires for terahertz wave guiding. Nature 2004;432:376–9.
[81] Li S, Jones RR. High-energy electron emission from metallic nano-tips driven by intense single-cycle terahertz pulses. Nat Commun 2016;7:13405.
[82] Du S, Yoshida K, Zhang Y, Hamada I, Hirakawa K. Terahertz dynamics of electron–vibron coupling in single molecules with tunable electrostatic potential. Nat Photon 2018;12:608–12.
[83] Park H, Park J, Lim AK, Anderson EH, Alivisatos AP, McEuen PL. Nanomechanical oscillations in a single-C60 transistor. Nature 2000;407:57–60.
[84] Zhang J, Zhao X, Fan K, et al. Terahertz radiation–induced subcycle field electron emission across a split-gap dipole antenna. Appl Phys Lett 2015;107:231101.
[85] Bagiante S, Enderli F, Fabiańska J, Sigg H, Feurer T. Giant electric field enhancement in split ring resonators featuring nanometer-sized gaps. Sci Rep 2015;5:8051.
[86] Hoffmann MC, Fülöp JA. Intense ultrashort terahertz pulses: generation and applications. J Phys D Appl Phys 2011;44:083001.
[87] Baek IH, Kang BJ, Uk Jeong Y, Rotermund F. Diffraction-limited high-power single-cycle terahertz pulse generation in prism-cut $LiNbO_3$ for precise terahertz applications. J Opt Soc Korea 2014;18:60–4.
[88] Lin HC, Ye PD, Wilk GD. Leakage current and breakdown electric-field studies on ultrathin atomic-layer–deposited Al_2O_3 on GaAs. Appl Phys Lett 2005;87:182904.
[89] Santos EJG, Kaxiras E. Electric-field dependence of the effective dielectric constant in graphene. Nano Lett 2013;13:898–902.
[90] Mertens J, Eiden AL, Sigle DO, et al. Controlling subnanometer gaps in plasmonic dimers using graphene. Nano Lett 2013;13:5033–8.
[91] Marinica DC, Kazansky AK, Nordlander P, Aizpurua J, Borisov AG. Quantum plasmonics: nonlinear effects in the field enhancement of a plasmonic nanoparticle dimer. Nano Lett 2012;12:1333–9.
[92] Ciracì C, Hill RT, Mock JJ, et al. Probing the ultimate limits of plasmonic enhancement. Science 2012;337:1072–4.
[93] Savage KJ, Hawkeye MM, Esteban R, Borisov AG, Aizpurua J, Baumberg JJ. Revealing the quantum regime in tunnelling plasmonics. Nature 2012;491:574–7.
[94] Esteban R, Borisov AG, Nordlander P, Aizpurua J. Bridging quantum and classical plasmonics with a quantum-corrected model. Nat Commun 2012;3:825.
[95] Huber R, Tauser F, Brodschelm A, Bichler M, Abstreiter G, Leitenstorfer A. How many-particle interactions develop after ultrafast excitation of an electron-hole plasma. Nature 2001;414:286–9.
[96] Kim J-Y, Kang BJ, Bahk Y-M, et al. Tunnelling current–voltage characteristics of angstrom gaps measured with terahertz time-domain spectroscopy. Sci Rep 2016;6:29103.
[97] Kang JH, Kim DS, Park QH. Local capacitor model for plasmonic electric field enhancement. Phys Rev Lett 2009;102:093906.
[98] Kyoung JS, Seo MA, Park HR, Ahn KJ, Kim DS. Far field detection of terahertz near field enhancement of sub-wavelength slits using Kirchhoff integral formalism. Opt Commun 2010;283:4907–10.
[99] Shalaby M, Merbold H, Peccianti M, et al. Concurrent field enhancement and high transmission of THz radiation in nanoslit arrays. Appl Phys Lett 2011;99:041110.
[100] Novitsky A, Zalkovskij M, Malureanu R, Lavrinenko A. Microscopic model of the THz field enhancement in a metal nanoslit. Opt Commun 2011;284:5495–500.
[101] Park HR, Park YM, Kim HS, et al. Terahertz nanoresonators: giant field enhancement and ultrabroadband performance. Appl Phys Lett 2010;96:121106.
[102] Asada M, Suzuki S, Kishimoto N. Resonant tunneling diodes for sub-terahertz and terahertz oscillators. Jpn J Appl Phys 2008;47:4375–84.
[103] Garcia-Vidal FJ, Martin-Moreno L, Ebbesen TW, Kuipers L. Light passing through subwavelength apertures. Rev Mod Phys 2010;82:729–87.
[104] Kang T, Kim RHJ, Choi G, et al. Terahertz rectification in ring-shaped quantum barriers. Nat Commun 2018;9:4914.
[105] Baltuska A, Udem T, Uiberacker M, et al. Attosecond control of electronic processes by intense light fields. Nature 2003;421:611–5.
[106] Rybka T, Ludwig M, Schmalz MF, Knittel V, Brida D, Leitenstorfer A. Sub-cycle optical phase control of nanotunnelling in the single-electron regime. Nat Photon 2016;10:667–70.